International Journal of Nanomedicine

Dovepress
open access to scientific and medical research

Open Access Full Text Article

ORIGINAL RESEARCH

# Preparation and Characterization Evaluation of Poly(L-Glutamic Acid)-g-Methoxy Poly(Ethylene Glycol)/Combretastatin A4/BLZ945 Nanoparticles for Cervical Cancer Therapy

Dongmei Guo[1], Yue Huang[2], Kun Wang[2], Chenguang Yang[2], Lili Ma[2], Yu Zhang[2], Haiyang Yu[2], Manhua Cui[1], Zhaohui Tang[2]

[1]Department of Gynecology and Obstetrics, The Second Hospital of Jilin University, Changchun, Jilin Province, 130041, People's Republic of China; [2]Key Laboratory of Polymer Ecomaterials, Changchun Institute of Applied Chemistry, Chinese Academy of Sciences, Changchun, 130022, People's Republic of China

Correspondence: Manhua Cui, Department of Gynecology and Obstetrics, The Second Hospital of Jilin University, 218 Ziqiang Road, Changchun, Jilin Province, 130041, People's Republic of China, Email cuimanhua@126.com; Yue Huang, Key Laboratory of Polymer Ecomaterials, Changchun Institute of Applied Chemistry, Chinese Academy of Sciences, Changchun, 130022, People's Republic of China, Tel/Fax +86 431 85262116, Email huangyue@ciac.ac.cn

---

**Purpose:** Cervical cancer (CC) is a highly vascularized tumor with abundant abnormal blood vessel, which could be targeted by therapeutic strategies. Poly(L-glutamic acid)-*g*-methoxy poly(ethylene glycol)/combretastatin A4 (CA4)/BLZ945 nanoparticles (CB-NPs) have shown great potential as nano vascular disrupting agents (VDAs) in the realm of synergistic cancer therapy.

**Methods:** In this study, we investigated the nanocharacteristics of CB-NPs, focusing on active pharmaceutical ingredients (API), as well as lyophilized samples combining API with protective agents (PAs). The in vivo efficacy of final sample (API + PAs) was evaluated.

**Results:** The assembled sphere of API with complex core and thin-shell structure was confirmed. PAs were found to significantly influence in vivo efficacy. Collaborative efforts between API and PAs, namely mannitol and lactose, resulted in the most promising lyophilized sample, ie, the final sample (FS2) for CC therapy. Impressively, FS2 demonstrated an exceptional 100% cure rate on the CC U14-bearing mice model.

**Conclusion:** FS2 has provided significant insights for cervical cancer therapy. It is also crucial to develop a comprehensive evaluation strategy for the formulation of nanomedicine, which has the potential to serve as a guideline for future clinical trials.

**Keywords:** combretastatin A4, BLZ945, glutamic acid, nano character, cervical cancer

---

## Introduction

Cervical cancer (CC) is one of the most common gynecological malignancies, ranking fourth in terms of both incidence and mortality.[1] In recent years, a notable rise in the incidence of CC, coupled with a trend toward affecting younger individuals, has become evident.[2] Owing to the early diagnosis and treatment, the survival time of CC patients was notably increased.[3] However, limited cure options are available for the sustained, recurrent, and transferred cases, leading to a subsequent poor prognosis.[4–6] For patients with unresectable CC, cisplatin (CDDP) is the most common chemical therapeutic option.[7–9] Unfortunately, CDDP did not benefit pelvic control or survival at the advanced stage of CC treatment.[10] CC is a highly vascularized tumor with abundant abnormal blood vessel, which could be targeted by therapeutic strategies.[11–15] Intravenous administration of vascular disrupting agents (VDAs) can selectively target endothelial cells, disrupt the established tumor vasculature, and then arrest tumor blood flow.[16–23]

An active VDA, combretastatin A4 (CA4), has been integrated into assembled nanoparticles, exemplified by poly (L-glutamic acid)-*g*-methoxy poly(ethylene glycol)/combretastatin A4/4-((2-(((1R,2R)-2-hydroxycyclohexyl)amino)

Received: 19 September 2023
Accepted: 12 November 2023
Published: 22 November 2023

## Graphical Abstract

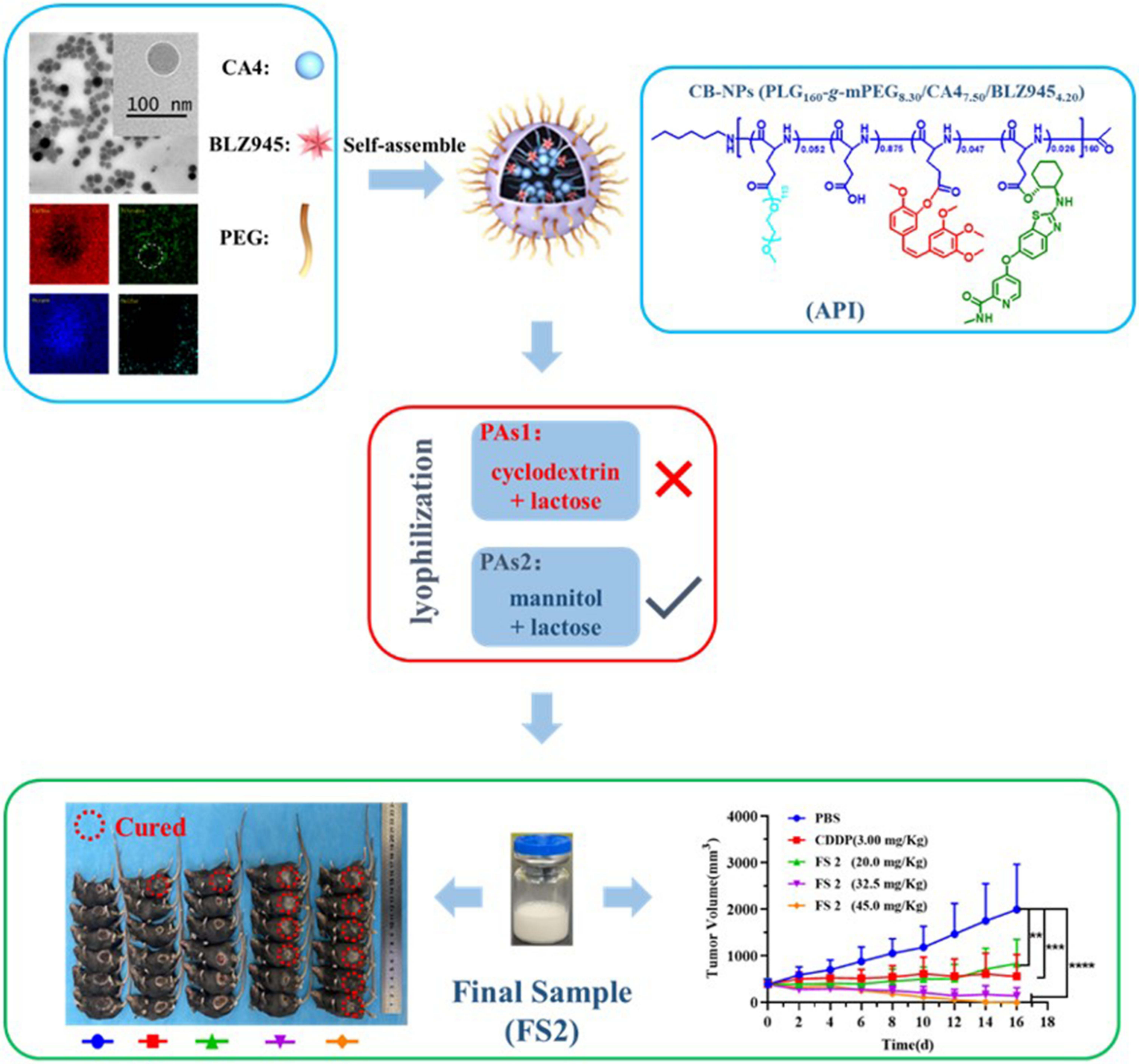

benzo[d]thiazol-6-yl)oxy)-N-methylpicolinamide (CB-NPs). This innovation owes its success to the cooperation of CA4 and 4-((2-(((1R,2R)-2-hydroxycyclohexyl)amino)benzo[d]thiazol-6-yl)oxy)-N-methylpicolinamide (BLZ945). Notably, CB-NPs, have demonstrated superior capabilities in targeting tumor vasculature and maintaining prolonged circulation within the body.[24] Specifically, the monofunctional VDAs-nanoparticles, poly(L-glutamic acid)-*g*-methoxy poly(ethylene glycol)/combretastatin A4 (C-NPs) have a low intratumoral permeability, resulting in excellent tumor vascular-targeting capability.[25–29] Furthermore, monotherapy of C-NPs could induce the polarization of tumor-associated macrophages (TAMs) toward the M2-like phenotype (M2-TAMs) and increase the infiltration of M2-TAMs, which may subsequently lead to tumor recurrence after treatment.[30–32] Therefore, the highly selective small molecular inhibitor of colony-stimulating factor receptor (CSF-1R) kinase, BLZ945, can be covalently bound to poly(L-glutamic acid) together with CA4 to obtain CB-NPs. CSF-1R inhibition by BLZ945 remarkably induces the infiltration of $CD8^+$ T cells and reduces the amounts of M2-TAMs in tumors. Our preliminary investigations have confirmed that CB-NPs loaded with CA4 and BLZ945 exhibit a synergistic therapeutic effect in the H22-bearing mice model.[33–36] Furthermore, the in vivo efficacy of CB-NPs is highly dependent on the ratio of active agents (AAs) (BLZ945/CA4), and loading content of AAs (BLZ945 + CA4). Then, a well-formulated CB-NPs with a B/C weight ratio of 0.45/1, and drug loading content (B + C) of 20.7 wt% ($PLG_{160}$-*g*-$mPEG_{8.30}$/$CA4_{7.50}$/$BLZ945_{4.20}$) was screened as the best candidate for clinical application.[37]

The in vivo fate of polymeric drugs could be determined by their nanocharacteristics, such as particle size, zeta potential, and morphology features.[38–41] The form of sample preparation of polymeric nanomedicine, such as tablets, capsules, and injections, plays a key role in a clinical trial because the active efficacy and toxicity are crucially influenced by preparing technology and adding agents.[42–47] For our proposed nanomedicine, the lyophilized technology is carried out to obtain a final sample of CB-NPs. The lyophilized sample should contain CB-NPs as active pharmaceutical ingredients (API), and protective agents (PAs). However, it is still unclear how the sample preparation, like technology and adding agents, could influence the final sample of CB-NPs.

Herein, CB-NPs with a confirmed formulation were synthesized and used as API to investigate the influence of sample form on the nanocharacteristics and in vivo efficacy. The fluorescent probe method, electron microscopy (EM), and dynamic light scattering (DLS) were carried out to confirm the nanocharacteristics of API (CB-NPs) and lyophilized sample (API + PAs). In vivo experimental results indicated that this type of PAs played a crucial role in efficacy and toxicity of the lyophilized sample. Improper addition of PAs could counteract the in vivo efficacy of API and increase sample toxicity dramatically. This phenomenon could be explained by the nanocharacteristics of API and lyophilized samples. In vivo efficacy test of lyophilized sample towards CC U14-bearing mice model showed that this optimized nanomedicine sample exhibited excellent antitumor efficacy, surpassing the performance of the positive drug, cisplatin. All the U14-bearing mice had been cured by the screened lyophilized sample FS2. This achievement suggests that the clinical adaptation disease of CB-NPs could be extended to a wider range of clinical conditions. This accomplishment signifies the development of a comprehensive evaluation strategy for the formulation of nanomedicine, which has the potential to serve as a guideline for future clinical trials.

# Materials and Methods

## Materials

The γ-benzyl-L-glutamate-N-carboxyanhydride (BLG-NCA) was purchased from Chengdu Enlai Biological Technology Co., Ltd., China. The crude product underwent two rounds of recrystallization from ethyl acetate and was then dried under vacuum at room temperature prior to use. Generally, 10 g BLG-NCA was dissolved in 100 mL ethyl acetate, then the solution of BLG-NCA was recrystallized in 100 mL hydrochloric acid solution (1 M) at −15 °C with the recovery rate of 65%. Methoxy poly(ethylene glycol) with a molecular weight (Mw) 5000 Da (mPEG5K) was obtained from J&K Scientific Co., Ltd. and dried by azeotropic distillation in toluene before use. N, N'-dimethylformamide (DMF) was stored over $CaH_2$ for 3 days and subsequently distilled under a vacuum prior to use. Combretastatin A4 (CA4) was purchased from Hangzhou Great Forest Biomedical Ltd., China. BLZ945 was obtained from Shanghai Bixi Chemical Co., Ltd., China. The 4-Dimethylaminopyridine (DMAP) was supplied by Aladdin Reagent Co. Ltd., China, and 2, 4, 6-trichlorobenzoyl chloride was obtained from Tianjin Heowns Biochemical Technology Co., Ltd., China. Hydroxypropyl-β-cyclodextrin, mannitol, and lactose were obtained from Energy Chemical Co., Ltd, China. All other reagents and solvents were purchased from Sinopharm Chemical Reagent Co., Ltd, China and used as received.

## Characterization

The synthetic routes of API were demonstrated in Scheme S1. Dynamic light scattering (DLS) data were measured by a zeta potential/size analyzer (Malvern, Nano-ZS, UK). The morphology feature of CB-NPs was confirmed by transmission electron microscopy (TEM) test (JEM-1400Flash, 120KV, Japan), high-resolution transmission electron microscopy (HRTEM) (JEM-F200, 200KV, Japan), and cryo-electron microscopy (cryo-EM) (Gatan-3200fsc, 300KV, America). Fluorescence data were collected using a fluorescence lifetime spectrometer (PTI, QM3000, USA).

## Cells and Animals

The murine hepatoma (H22) cancer cell line was obtained from BeNa Culture Collection Co. Ltd., China. Cervical cancer U14 cancer cell line was obtained from Fu Heng Biology Co. Ltd., China. H22 cells were cultured in RPMI-1640 (containing 10% fetal bovine serum (FBS), 100 U/mL penicillin and 100 μg/mL streptomycin) at 37 °C in an atmosphere of 5% $CO_2$. U14 cells were cultured in DMEM (containing 10% fetal bovine serum (FBS), 100 U/mL penicillin and 100 μg/mL streptomycin), and maintained under similar culture conditions. Female BALB/c, C57, and BALB/c nude mice (6–8 weeks old) with an average body weight of 16–18 g were obtained from Beijing Vital River Laboratory Animal Technology Co., Ltd. All animals received proper care in compliance with the guidelines specified in the "Guide for the Care and Use of Laboratory Animals". Additionally, all procedures were approved by the Animal Care and Use Committee of Changchun Institute of Applied Chemistry, Chinese Academy of Sciences.

## Preparation of API and Final Sample

CB-NPs ($PLG_{160}$-g-$mPEG_{8.30}$/$CA4_{7.50}$/$BLZ945_{4.20}$) with pre-determined AAs ratios and contents were prepared as active pharmaceutical ingredients (API) according to our previous work.[37] The $^1H$ NMR, Gel permeation chromatography (GPC), and high-performance liquid chromatography (HPLC) spectra of API are shown in Figure S1. The API was lyophilized with certain kinds of protective agents (PAs). The freeze-dried powder was obtained as final samples (FSs), as shown in Scheme 1.

## Nanocharacteristics of API and Final Sample

The critical micelle concentration (CMC) of API was determined by the fluorescent probe method. A fluorescent probe, pyrene (10.11 mg, 50 mmol) was dissolved into 50 mL methylbenzene. A methylbenzene solution (10 μL) was added into 9 volumetric flasks (5 mL). After volatilization of methylbenzene, the API solution (5 mg/mL) was added into the flasks (5 mL) at a series of volumes: 5.00, 2.50, 1.25, 1.00, 0.60, 0.45, 0.30, 0.15, and 0.08 mL. Subsequently, these flasks were measured by a fluorescence lifetime spectrometer with an excitation wavelength of 334 nm and an absorption wavelength range of 360–600 nm. For size distribution, API and FSs were dissolved into deionized water for 10 min, and the size of API and FSs in water solution was measured by a zeta potential/size analyzer (Malvern Zetasizer Nano ZS).

For microscopic characterization, API and FSs were, respectively, dissolved into deionized water to form solutions. After 24 h, a drop of solution was dripped onto the copper grid and allowed to air dry. This prepared sample was then subjected to TEM

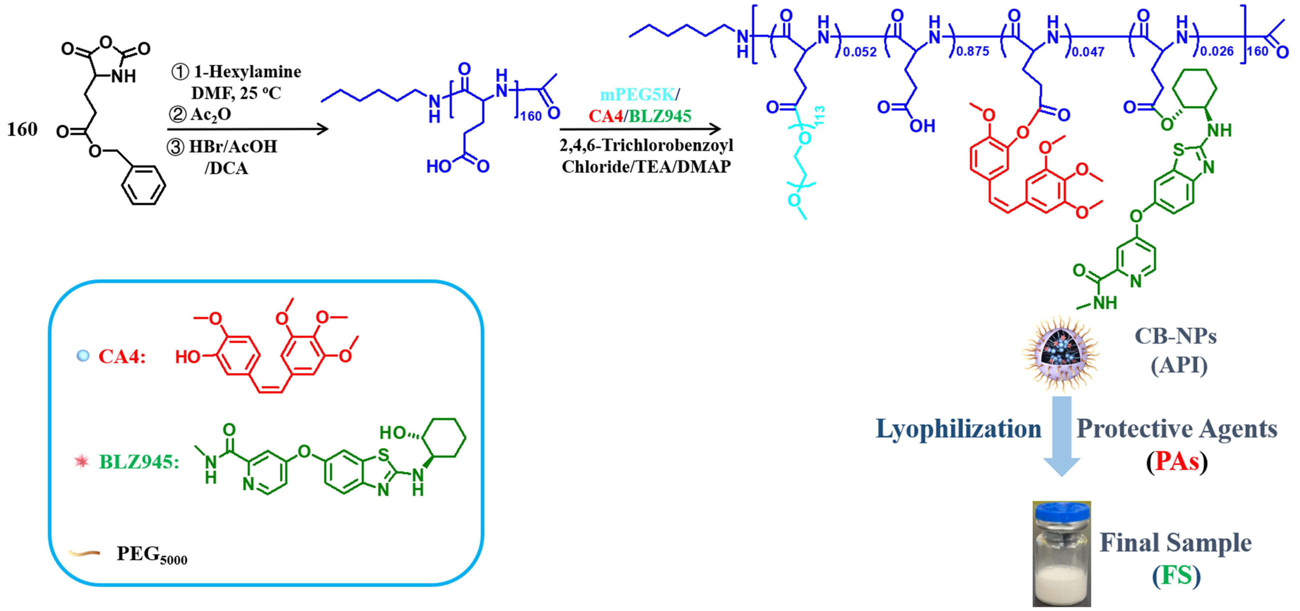

**Scheme 1** The preparation of API and FS.

and HRTEM testing. For TEM imaging, a minute amount of sample solution (normally 3 μL) was coated on a carbon-coated grid. The grid was rapidly immersed in liquid propane that had been cooled using liquid nitrogen. To preserve the structural integrity of the solutions and to capture accurate micro-structures, all grid manipulation and transfer processes were conducted within a liquid nitrogen environment. Subsequently, cryo-EM was employed to capture the microstructures of the API.

## In vivo Antitumor Efficacy Test for FSs

The H22 subcutaneous tumor model was generated by subcutaneously injecting the right flank of H22 mice with an inoculum size of $2\times10^6$ H22 cells, which were then maintained by an intraperitoneal passage in the mice. When the tumor volume reached approximately 200 $mm^3$, the mice were randomly allocated to the required groups (n = 6) and subjected to treatment using the formulated samples. The subcutaneous tumor model of U14 cervical cancer was established by following the work of Gu and Chen.[48,49] Tumor volume and body weight were used to assess the treatment efficacy and systemic toxicity, respectively. The tumor volume was calculated by the following formula:

$$\text{Tumor volume}(\text{V}) = \text{a} \times \text{b}^2/2$$

Where a and b stand for the longest and shortest diameters of the tumors, respectively, measured using vernier calipers. The tumor inhibition rate ($E_s$) of the sample was calculated using the following formula:

$$E_s = \left(1 - \frac{TV_s - T_0}{TV_c - T_0}\right) \times 100\%$$

Where $TV_s$ and $TV_c$ are the average tumor volume of the sample and control group, respectively. $T_0$ was the initial tumor volume on Day 0.

## Hematoxylin and Eosin (H&E) Staining

Tumors and/or the main organs (heart, liver, spleen, lung, kidney) were excised from mice and fixed in 4% buffered paraformaldehyde for 24 h. All the tissues were embedded in paraffin, sliced to a thickness of 5.0 μm, and then stained with H&E to evaluate the histopathological changes under a microscope (Nikon TE 2000U).

## Maximal Tolerable Dose (MTD) of Final Sample

BALB/c, C57, and BALB/c nude mice were randomly divided into several groups (n = 4, female, average weight: 18.0 ± 2.0 g; mean ± SD). FS was administered intravenously via the tail vein following the dose ranging from 30 mg/kg to 65 mg/kg (on a CA4 basis). The survival rates and body weight changes were recorded every day. Then, the MTD of FS for BALB/c, C57, and BALB/c nude mice were determined.

## Pharmacodynamic Experiment of Final Sample

The CC U14 subcutaneous tumor model was generated by subcutaneously injecting the right flank of mice with an inoculum size of $3\times10^6$ U14 cells. The C57 mice bearing U14 tumor (tumor volume: 300–500 $mm^3$; n = 6) were randomly divided into 5 groups and treated with designed drugs. The intravenous (i.v.) injection frequency of the final sample was adjusted according to the body weight loss of MTD data. CDDP was introduced as a positive control drug for the bearing mice model.

## Statistical Analysis

Data were expressed as the mean ± SD. Statistical significance was determined using one-way ANOVA. Differences were considered statistically significant when $P<0.05$ and highly significant when $P<0.01$.

# Results and Discussion

## CMC Value Determination of API

The CMC value of CB-NPs (API) is an important indicator of the nanomedicine characteristics. To determine the CMC value of API, the pyrene fluorescence probe method was employed. Typically, pyrene exhibits five steady-state fluorescence peaks. The intensity ratio of peak 1 ($\lambda_1$: 372) to peak 3 ($\lambda_3$: 384) ($I_1/I_3$) is highly sensitive to changes in solvent polarity, which often experiences a significant alteration near the CMC value of API. Figure 1A shows the emission spectra of pyrene at different concentrations of API. The fluorescence emission spectra of pyrene were strongly influenced by the concentration of API. Spectra with clear characteristic peaks were observed during low API concentrations (<1.00 mg/mL). At concentrations exceeding 1.00 mg/mL, the spectra showed a disappearance of characteristic peaks and a notable blue shift. This phenomenon could be attributed to the escalating turbidity of the API solution resulting from the elevated concentration. Figure 1B shows the $I_1/I_3$ values as a function of API concentration. An evident decrease in $I_1/I_3$ value was observed, exhibiting a significant change. The CMC value of API was determined to be 0.40 mg/mL, identified as the concentration corresponding to the abrupt midpoint of the $I_1/I_3$ curve.[50,51]

## Size Character and Morphologic Study of API

The nanocharacteristics such as aggregation behavior and size distribution of API were studied near the CMC value. Figure 2 shows the DLS and TEM results of API at the concentration of 0.40 mg/mL. As shown in Figure 2A, the API solution had a unimodal distribution shortly after preparation (within 72 h). However, when the preparation time exceeded 96 h, a bimodal distribution was observed, which may be due to the unstable nanocharacteristics of API. TEM images Figure 2B showed that the API assembled into spherical morphology in water, consistent with micellar characteristics. The micellar size of API ranged from 20 to 80 nm, aligning with the findings from the DLS measurement. These results confirm that the API can form spherical micelles in water spontaneously. However, individual micelles are unable to sustain a stable nano size over extended periods. Therefore, the API should be prepared into a freeze-dried powder for the final sample. In this context, the exploration and investigation of incorporating certain additives, like PAs, become imperative.

To further investigate the nanocharacteristics of API, HRTEM and cryo-EM were carried out. As shown in Figure 2C, the HRTEM image of API revealed a distinctive spherical core-shell structure, featuring numerous dark points within the core. This indicates that the hydrophobic CA4 and BLZ945 constituted the core of API, while $PEG_{5000}$ formed the shell of the micelle. The Cryo-EM image (Figure 2D) provided visual evidence confirming the core-shell structure. The thin-shell size realm of 8–12 nm, and 40–60 nm core could be determined by the Cryo-EM results. To further explore the nature of the dark points within the core, an element mapping test (Figure 2E) was conducted to examine the stack mode of CA4 and BLZ945. The element mapping images revealed the presence of carbon (C), nitrogen (N), oxygen (O), and sulfur (S) elements. Notably, C and O demonstrated a uniform distribution. Interestingly, N displayed a non-uniform distribution within the core, with a noticeable absence of N in a specific area (indicated by the white dotted circle), which closely aligned with the dark point within the core. This may be due to the internal stack of CA4, which lacks N. Conversely, S, present

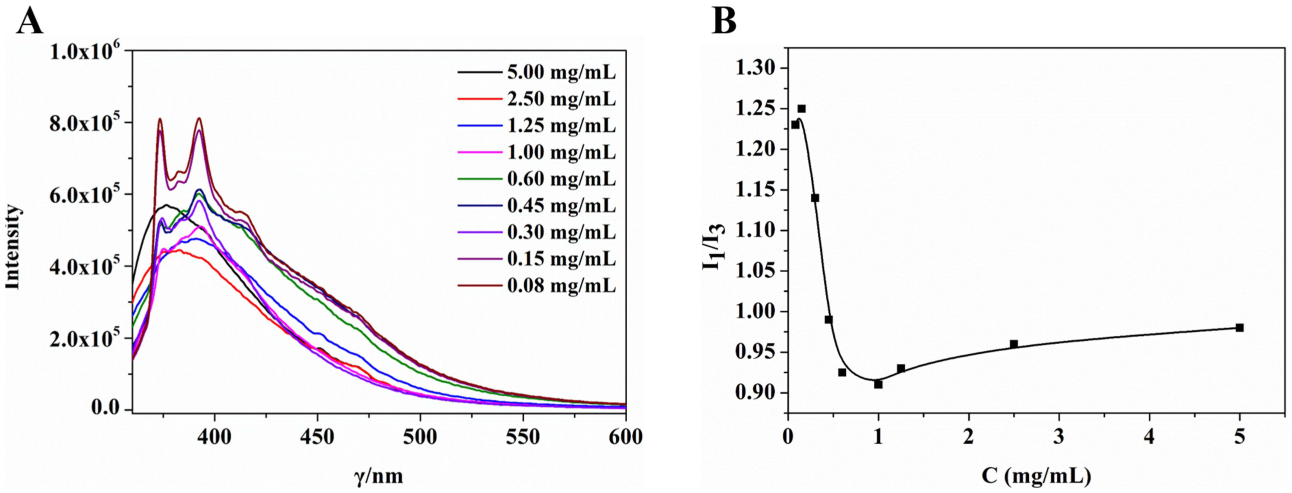

**Figure 1** The pyrene fluorescence probe method testing results for the CMC value of API. (**A**) The emission spectra of pyrene at different concentrations of API; (**B**) $I_1/I_3$ values of emission spectra as a function of the API concentration.

solely in BLZ945 (Figure 2F), exhibited a cyclic distribution, potentially indicating the distribution pattern of BLZ945 within the core. The self-assembling mode of API is shown in Figure 2F: a core composed of partially stacked CA4 and cyclically distributed BLZ945, surrounded by the PLG-mPEG shell of the micelle.

## Determination of PAs for Final Sample

Given that the final sample will be prepared as a freeze-dried powder, a thorough examination of the PAs was conducted to facilitate the sample preparation process. DLS was used to inspect the nanocharacteristics of the sample solution during the lyophilization process. Two types of PAs, cyclodextrin (2%) + lactose (3%) and mannitol (2%) + lactose (3%), were chosen because of their excellent protective function and stable ability. Figure 3 shows the DLS results of API within the lyophilization process, revealing that API added with either PAs1 or PAs2 maintains a unimodal distribution after the lyophilization process. Additionally, the DLS data of the re-soluble solution containing API and PAs demonstrated a sustained unimodal distribution at least 72 h. The in vivo efficacy of the final sample (FS) that contained API and PAs was then explored.

The H22 tumor-bearing mice were intravenously injected with API, and FSs when the tumor volume reached 200 mm$^3$ (hereafter "Day 0"). Figure 4 shows the effect of each treatment on the in vivo efficacy of the H22 tumor-bearing mice model. The therapy regimen is shown in Figure 4A. The concentration of FS was confirmed by HPLC, and

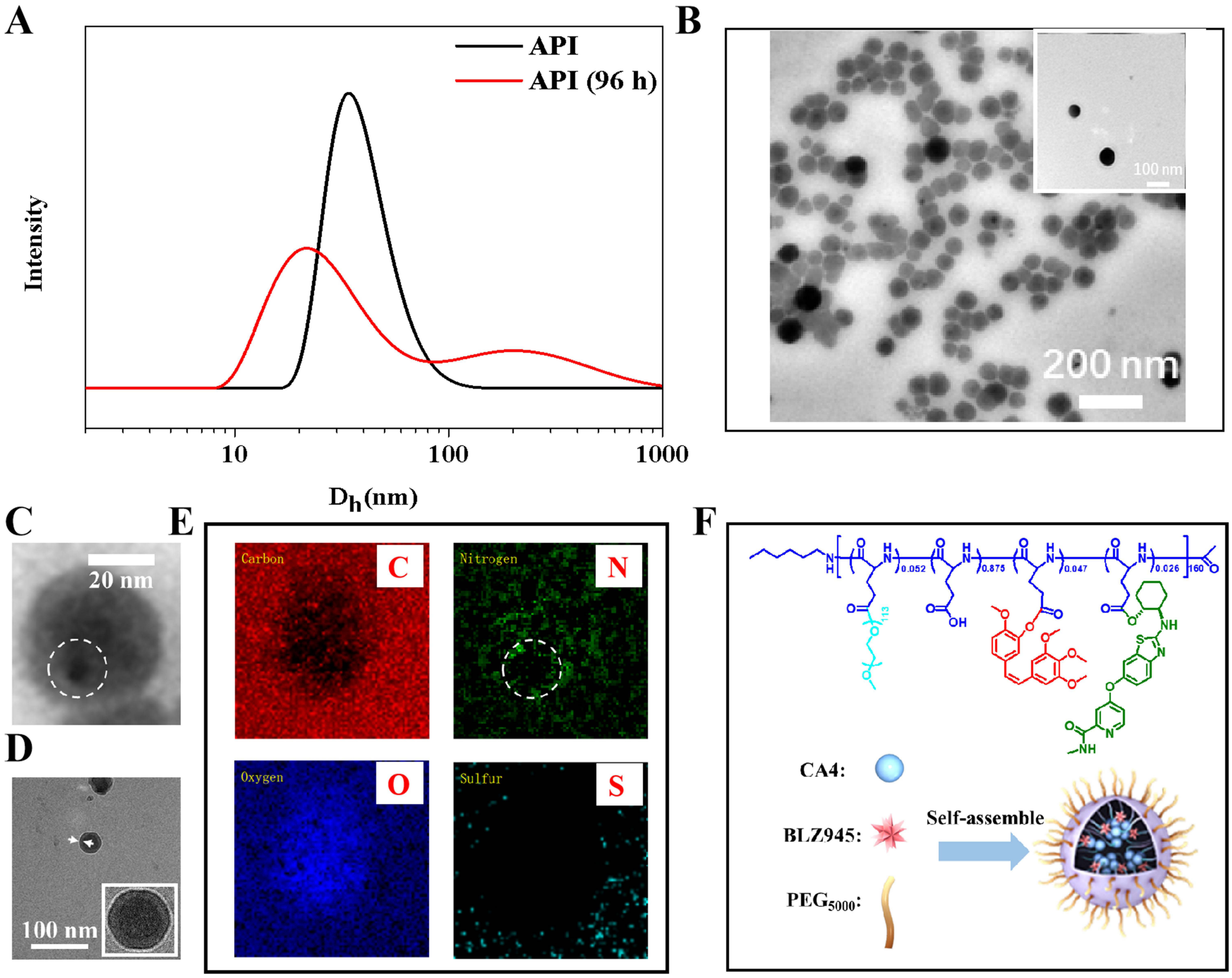

**Figure 2** Nano morphology and self-assembling behavior of API. (**A**) DLS results of API solution at the concentration of 0.40 mg/mL as a function of time; (**B**) TEM images of the API solution at the concentration of 0.40 mg/mL; (**C**) The HRTEM image of API; (**D**) The Cryo-EM image of API; (**E**) Element (C, N, O, and S) mapping images of API; (**F**) The self-assembling illustration of API.

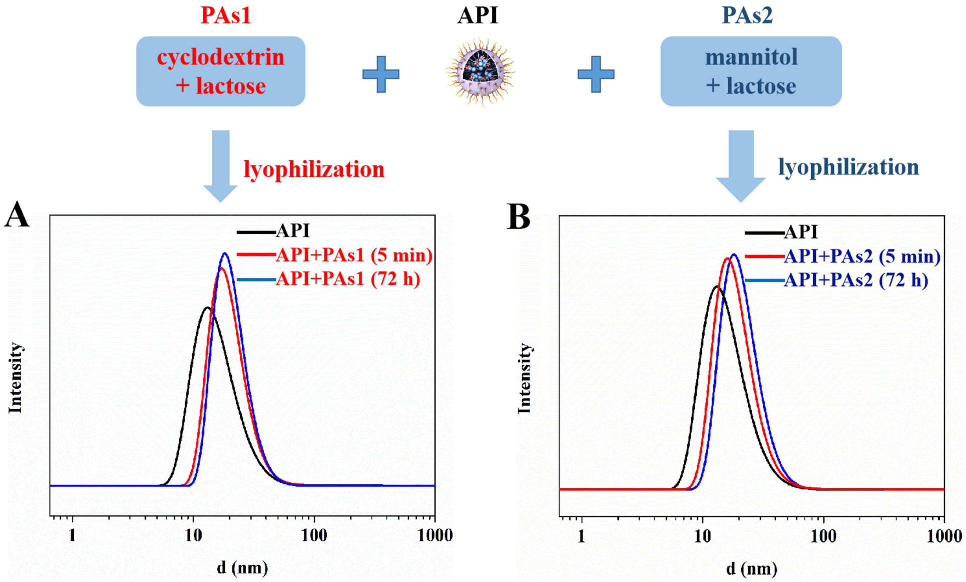

**Figure 3** DLS measurements of the API solution and re-soluble solution of lyophilized powder (API+PAs). (**A**) DLS measurements of the API solution and API+PAs1 solution at different times (5 min, 72 h); (**B**) DLS measurements of the API solution and API+PAs2 solution at different times (5 min, 72 h).

the injection dosage was determined based on CA4. Interestingly, the performance of FS with different PAs varied dramatically in terms of in vivo efficacy toward the H22 model. As shown in Figure 4B, FS1 with cyclodextrin and lactose as PAs exhibited lower antitumor efficacy compared to both API and FS2. Furthermore, concerning FS1, an unfortunate occurrence of death cases was observed after the second injection. All the mice treated with FS1 died between Day 8 and Day 10. Hematoxylin and eosin (H&E) staining of the main metabolic organs from the deceased mice (Figure 4D) highlighted noticeable bleeding in organs rich in blood vessels, such as the liver, spleen, and lungs (indicated by red arrows). The liver staining revealed focal necrosis of hepatocytes, nucleolysis (yellow arrow), sporadic lymphocyte infiltration (blue arrow), and extensive dilatation of the hepatic sinuses (black arrow). These staining observations remarkably corresponded with the phenomenon of burst release of CA4, possibly influenced by the alteration in CA4 release behavior due to the secondary structure of cyclodextrin. By contrast, FS2 with mannitol and lactose as PAs maintained comparable antitumor efficacy compared to that of API, and no death occurred during the entire treatment period. The decline in body weight for FS2 was consistent with the API treatment (Figure 4C). These findings underscore the crucial impact of PAs on the in vivo efficacy of nanomedicine. According to the results obtained in the experiment, mannitol (2 wt%) + lactose (3 wt%) were, identified as the suitable PAs for the final sample (FS2).

## MTD of Selected FS

With the preceding sections' results establishing FS2 as the optimal final sample for clinical applications, further comprehensive evaluations were conducted to determine its preclinical parameters, including MTD, and clinical indications. Although the MTD value of API toward BALB/c had been studied by our previous work, MTD investigations specific to FS2 were lacking. In this study, we recorded the changes in body weight and survival curves of BALB/c mice, C57 mice, and BALB/c nude mice at different injection dosages of FS2 (on CA4 basis).

As shown in Figure 5A and B, no fatalities were observed at dosages below 40.8 mg/kg, and the body weight of the two groups treated with a dosage below 40.8 mg/kg was recovered within 6–8 days. A few instances of death were recorded within the injection dosage range of 40.8 to 50.1 mg/kg. At the injection dosage rose of 55.4 mg/kg, all mice died in a short time (<4 d). The MTD value of FS2 in BALB/c mice was determined to be 40.8 mg/kg, an improvement over the API's MTD value of 33.0 mg/kg. Figure 5C and D show that no deaths occurred within the injection dosage range of 25.9 to 55.0 mg/kg. The body weight of all the groups was recovered within 4–6 days. However, at an injection dosage of 48.2 mg/kg, the body weight loss of C57 mice exceeded 20%, indicating a critical tolerance limit of 48.2 mg/

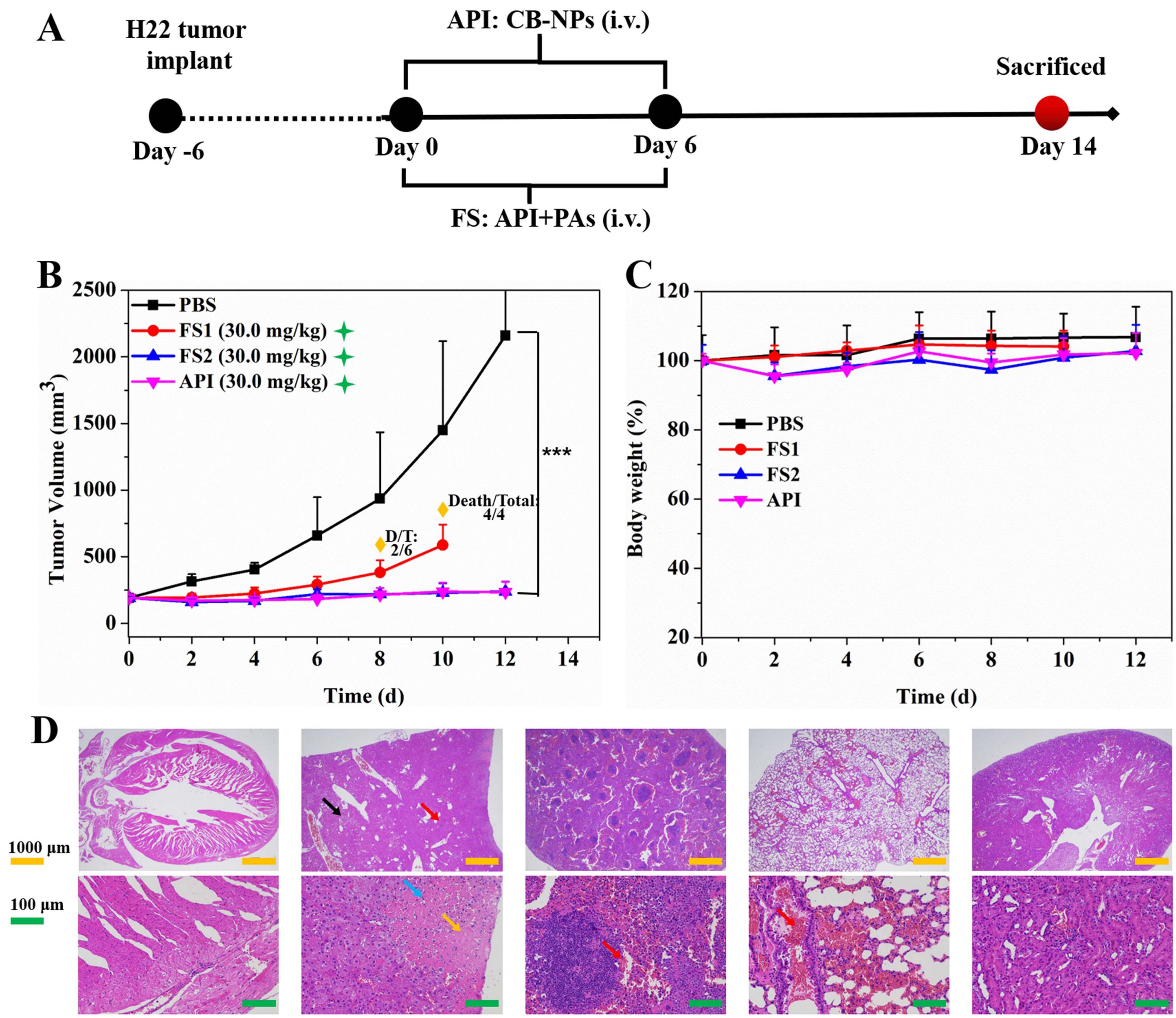

**Figure 4** In vivo efficacy of API and FSs in the H22 tumor-bearing mice model. (**A**) Therapy regimen; (**B**) Tumor volume relative to the start point as a function of time; (**C**) body weight relative to the start point as a function of time. The arrows represent the day on which the i.v. injection via tail vein was performed. The yellow diamond shape represents the death detail of mice treated with FS1. The green star shape stands for the injection concentration that was prepared based on CA4. The data are shown as mean ± SD (n = 6), ***P < 0.001; (**D**) H&E staining of main metabolic organs of deceased mice treated with FS1.

kg for C57 mice toward FS2. Figure 5E and 5F show that for the BALB/c nude, no death occurred at the injection dosage ranging from 45.0 to 60.0 mg/kg. The body weight of all groups rebounded within 3 days. The body weight loss of BALB/c nude remained below 11.0%. However, at an injection dosage of 65.0 mg/kg, some instances of death were recorded. Thus, the critical tolerance of BALB/c nude toward FS2 was 60.0 mg/kg. These results highlight distinct tolerance levels of different mouse strains to FS2, offering valuable clinical indications for the use of CB-NPs as nanomedicine.

## Pharmacodynamic of Selected FS

To better understand the pharmacodynamics of FS2, further investigations were conducted on U14-bearing C57 mice, with CDDP as the positive drug. The therapy regimen is shown in Figure 6A. At Day 0, the initial tumor volume was approximately 400 mm$^3$, and the injection concentration was prepared based on CA4 dosage. The i.v. frequency of FS2 was 5 days once, which based on the MTD value of FS2 toward C57 mice. The i.p. frequency of CDDP was 3 days once time. All the groups were sacrificed on day 17.

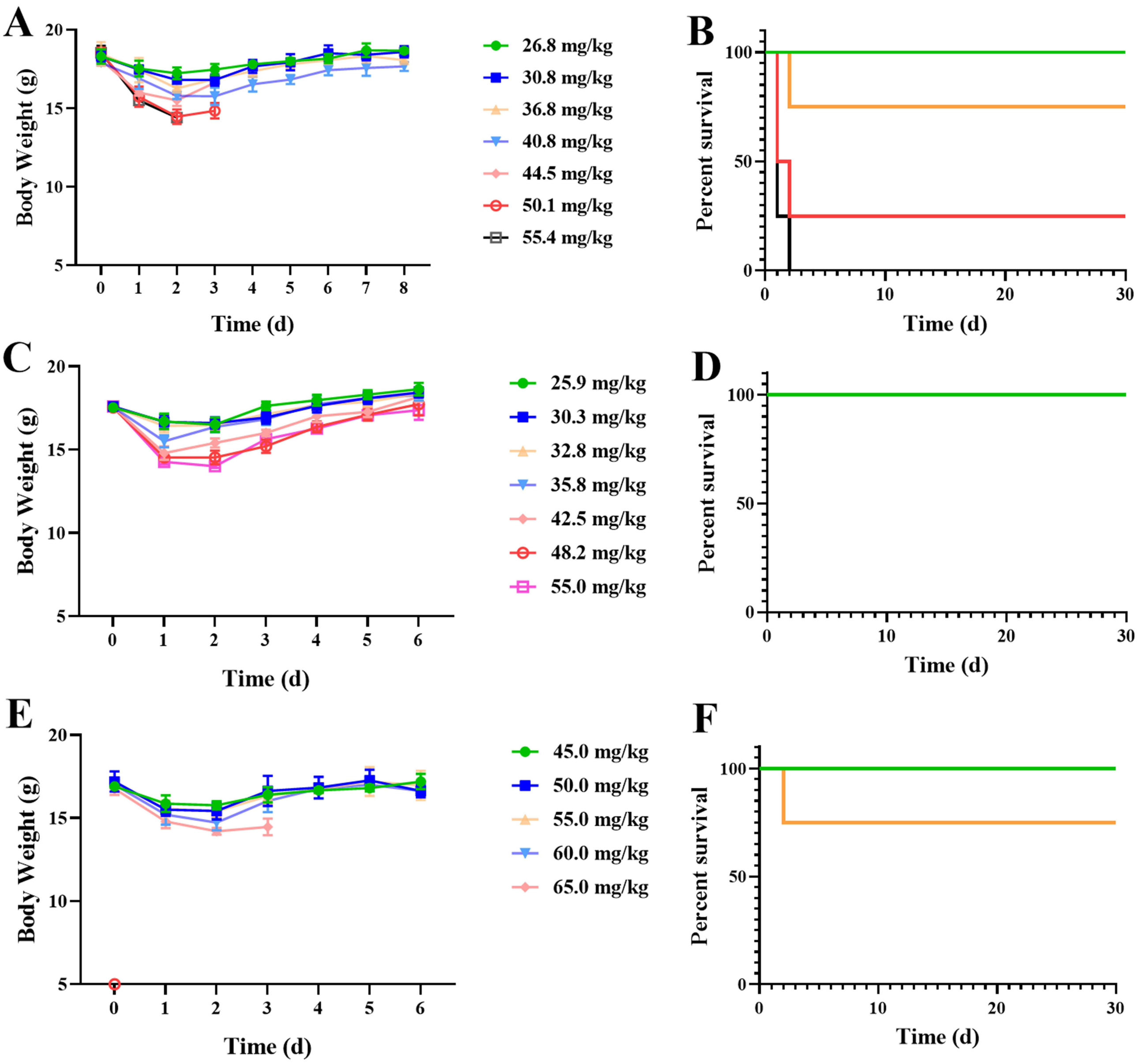

**Figure 5** The changes in body weight and survival curves of injection groups toward (**A** and **B**) BALB/c mice, (**C** and **D**) C57 mice, and (**E** and **F**) BALB/c nude as the function of dosage (on CA4 basis).

Figure 6B and C show the change in tumor volume and body weight over time for various therapy regimens, relative to the starting point. As shown in Figure 6B and C, the antitumor ability of FS2 was excellent, with a clear dose-dependent relationship observed among the three FS2 groups. In comparison to PBS, the FS2 (20.0 mg/kg) and CDDP groups demonstrated a significant tumor inhibitory effect, with the E value reaching 72.4% and 89.5%, respectively. Notably, a significant proportion of U14 model mice in the 32.5 mg/kg FS2 group experienced a cure rate of 67.0%, and all cases in the 45.0 mg/kg group were cured (cure rate: 100%). These two treatments showed superior tumor inhibition effects compared to the control and positive drug groups.

Remarkably, for the initial volume of tumor near 400 mm$^3$, the E value of the FS2 group (20.0 mg/kg) was 72.4%. As previously validated in our work, the starting dose (SD) of FS2 was defined as the dosage demonstrating a 60% inhibition effect (E) compared to the blank injection.[37] Therefore, the SD value of FS2 toward the U14-bearing C57 mice model was less than 20.0 mg/kg. Body weight loss across all mice in the FS2 groups was less than 20%, indicating modest

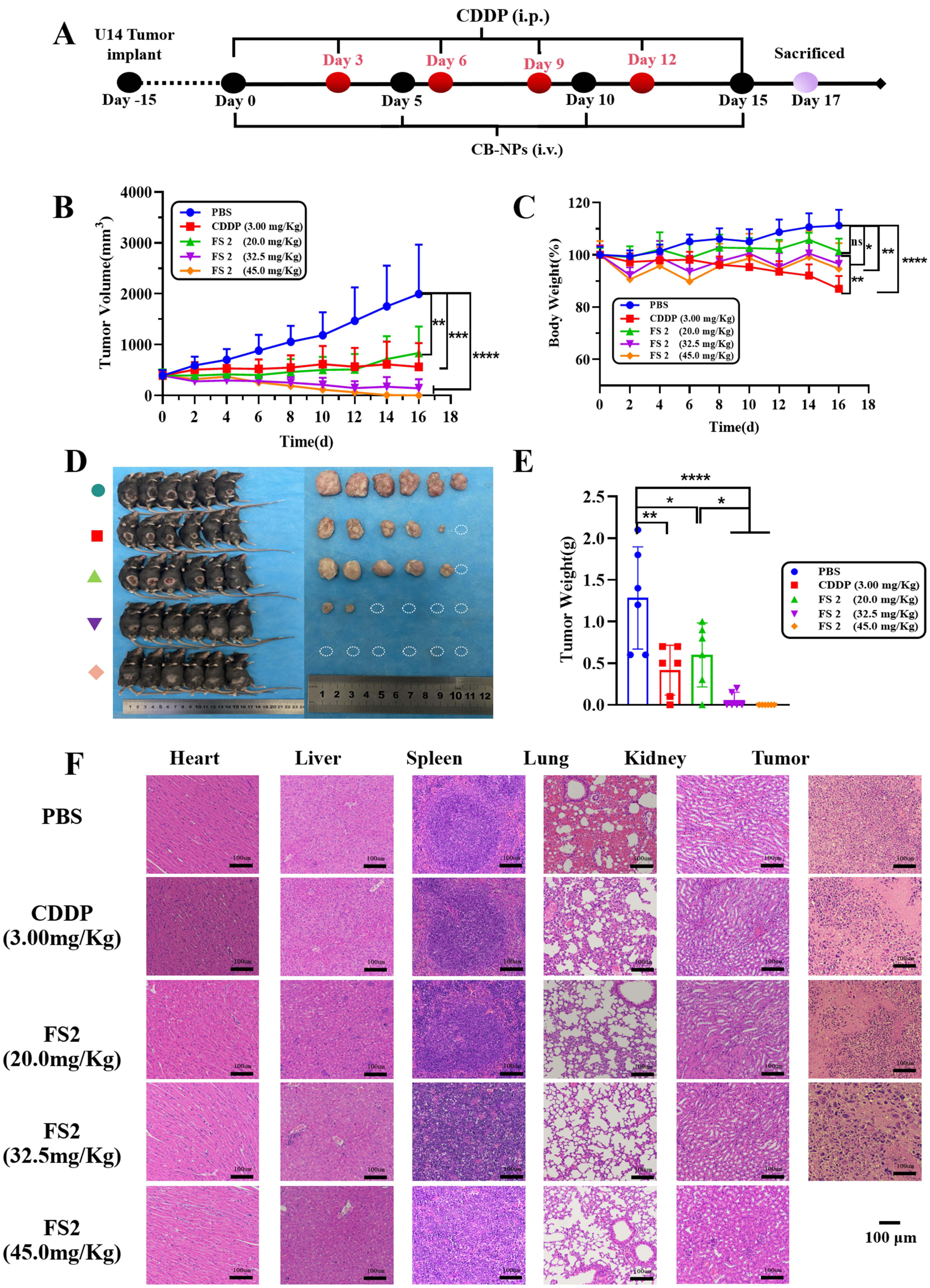

**Figure 6** Pharmacodynamic results of designed groups on U14-bearing mice. (**A**) Therapy regimen; (**B**) mean tumor size; (**C**) body weight; (**D**) mice and tumor images; (**E**) tumor weight of subcutaneous U14 tumor in PBS, CDDP, and FS2 groups (n = 6); (**F**) H&E staining of main metabolic organs of PBS, CDDP, and FS2 groups. Data were presented as means ± SD (n = 6), $^*P < 0.05$, $^{**}P < 0.01$, $^{***}P < 0.001$, $^{****}P < 0.0001$.

toxicity of the nanomedicine at given dosages. By contrast, the positive drug CDDP exhibited unacceptable body weight loss (exceeding 20%) after Day 12 (Figure 6C).

Figure 6D shows the mice and tumor images on Day 17. A cured case was observed in both the CDDP and FS2 (20.0 mg/kg) groups. In the FS2 (32.5 mg/kg) group, four out of six mice were cured, while all mice in the FS2 (45.0 mg/kg) group achieved a cure. The tumor weight (Figure 6E) of all groups at the end of the experiment revealed significant anticancer effect within the FS groups compared to the control and positive drug groups. Figure 6F demonstrated the H&E staining of the main organs and tumors of all groups. The reason for the lack of tumor staining in FS2 (45mg/kg) was owe to its 100% cure rate. No significant bleeding or structural changes were found in the main metabolic organs between the PBS and FS2 treatment groups. In terms of tumor staining, large areas of tumor necrosis were observed in the FS2 treatment groups. In the FS2 (32.5 mg/kg) tumor cells, a significant amount of nuclear fragmentation was observed. These pharmacodynamics findings hold the potential to provide valuable guidance for clinical applications.

## Conclusion

To facilitate the development of nanomedical drugs, it is crucial to conduct thorough and meticulous studies on nano characterization. The aim of our paper is to provide valuable insights for the clinical research of nanomedical drugs by utilizing multiple characterization methods, with a particular focus on the EM-mapping test. This will help to clearly elucidate the nanocharacteristics and aggregation behavior of CB-NPs. In this work, we successfully formulated a nanomedicine sample containing CB-NPs as active pharmaceutical ingredients (API), along with the mannitol and lactose as PAs. This enabled us to determine the optimal formula of CB-NPs as nanomedicine. The final sample (FS) of this nanomedicine in the form of lyophilized injection powder was verified. Several nanocharacteristics including CMC value, size, and morphology of API and FS were examined to serve as the indicator of the nanomedicine preparation process. The assembled sphere of API with complex core and thin-shell structure was confirmed by visually EM testing methods. Interestingly, the in vivo efficacy of API (CB-NPs) in combating cancer is dramatically affected by PAs. Transitioning from mannitol to cyclodextrin as PAs could lead to a reversal of the in vivo effects of the API from positive to negative.

A comprehensive medicine-screening strategy was established based on in vivo evaluation. This strategy played a pivotal role in identifying the optimal FS2 (API = CB-NPs, PAs = mannitol (2 wt%) + lactose (3 wt%)). FS2 maintained the potent antitumor activities of API while having an acceptable toxicity profile similar to the API itself. Consequently, FS2 could be used as lyophilized intravenous injection powder in clinical applications. Detailed preclinical parameters, including the Maximum Tolerated Dose (MTD) value of FS2 for three different species of mice, were meticulously determined. Importantly, FS2 displayed varying MTD values across distinct mouse species.

To expand the clinical indications of FS2, we further investigated the in vivo efficacy using a CC U14-bearing mice model. Remarkably, FS2 at concentrations above 20.0 mg/kg exhibited an inhibition rate (E) of higher than 70.0%. More importantly, FS2 also demonstrated an excellent cure rate (CR) at concentrations higher than 20.0 mg/kg ($CR_{32.5\ mg/kg}$ = 67%, $CR_{45.0\ mg/kg}$ = 100%). Furthermore, FS2 exhibited superior anticancer efficacy against larger U14 tumors (400 $mm^3$) in comparison to the positive drug CDDP. The FS2 demonstrated outstanding anti-cervical cancer efficacy while exhibiting low levels of toxicity, making it a promising candidate for clinical anti-tumor therapy. Our research highlights the potential of FS2 as a new and effective anti-tumor drug, offering hope for better treatment options for cancer patients.

## Acknowledgment

This work is financially supported by the Ministry of Science and Technology of China (2022YFE0110200), National Natural Science Foundation of China (52103195, 52025035, 81772772).

## Disclosure

The authors report no conflicts of interest in this work.

# References

1. Hyuna Sung JFM, Siegel RL, Laversanne M, Isabelle Soerjomataram MD, Ahmedin Jemal DMV, Bray BSc F. Global cancer statistics 2020: GLOBOCAN estimates of incidence and mortality worldwide for 36 cancers in 185 Countries. *CA Cancer J Clin*. 2021;71(209–249):209. doi:10.3322/caac.21660
2. Yin L, Lu S, Zhu J, Zhang W, Ke G. Ovarian transposition before radiotherapy in cervical cancer patients: functional outcome and the adequate dose constraint. *Radiat Oncol*. 2019;14(1):100. doi:10.1186/s13014-019-1312-2
3. Monk BJ, Enomoto T, Kast WM, et al. Integration of Immunotherapy into Treatment of Cervical Cancer: recent Data and Ongoing Trials. *Cancer Treat Rev*. 2022;106:102385. doi:10.1016/j.ctrv.2022.102385
4. Kitagawa R, Katsumata N, Shibata T, et al. Paclitaxel plus carboplatin versus paclitaxel plus cisplatin in metastatic or recurrent cervical cancer: the open-label randomized phase III trial JCOG0505. *J Clin Oncol*. 2015;33(19):2129–2135. doi:10.1200/JCO.2014.58.4391
5. Maria Kyrgiou AA, Arbyn M, Lax SF, et al. Terminology for cone dimensions after local conservative treatment for cervical intraepithelial neoplasia and early invasive cervical cancer: 2022 consensus recommendations from ESGO, EFC, IFCPC, and ESP. *Lancet Oncol*. 2022;23 (8):385–392. doi:10.1016/S1470-2045(22)00191-7
6. Du S, Yan J, Xue Y, Zhong Y, Dong Y. Adoptive cell therapy for cancer treatment. *Exploration*. 2023;3:4. doi:10.1002/EXP.20210058
7. Brozovic A, Osmak M. Activation of mitogen-activated protein kinases by cisplatin and their role in cisplatin-resistance. *Cancer Lett*. 2007;251 (1):1–16. doi:10.1016/j.canlet.2006.10.007
8. Zhang Z, Zhang S, Lin B, Wang Q, Nie X, Shi Y. Combined treatment of marizomib and cisplatin modulates cervical cancer growth and invasion and enhances antitumor potential in vitro and in vivo. *Front Oncol*. 2022;12:974573. doi:10.3389/fonc.2022.974573
9. Feng Y, Wang J, Cao J, Cao F, Chen X. Manipulating calcium homeostasis with nanoplatforms for enhanced cancer therapy. *Exploration*. 2023. doi:10.1002/EXP.20220173
10. Pearcey R, B. M, Drouin P, et al. Phase III trial comparing radical radiotherapy with and without cisplatin chemotherapy in patients with advanced squamous cell cancer of the cervix. *J Clin Oncol*. 2002;20(4):966–972. doi:10.1200/JCO.2002.20.4.966
11. Sha Chen HB, Miao Y, Liu F, Zhang L. Clinical value of transvaginal color Doppler ultrasound in evaluating angiogenesis of cervical cancer. *J Med Imaging*. 2022;32(7):1254–1257.
12. Shiliang Xu BB. Research of three-dimensional energy imaging detects cervical cancer and pathologic MVD. *Chinese J Ultrasound Med*. 2017;33 (9):816–819.
13. Tozer GM, K. C, Bruce C. Baguley disrupting tumour blood vessels. *Nat Rev Cancer*. 2005;5:423–435. doi:10.1038/nrc1628
14. Winn BA, Devkota L, Kuch B, et al. Bioreductively activatable prodrug conjugates of combretastatin A-1 and combretastatin A-4 as anticancer agents targeted toward tumor-associated hypoxia. *J Nat Prod*. 2020;83(4):937–954. doi:10.1021/acs.jnatprod.9b00773
15. Hong S, Huang Q-X, Ji P, et al. Vascular disrupting agent-induced amplification of tumor targeting and prodrug activation boosts anti-tumor efficacy. *Sci China Chem*. 2022;65(10):1994–2004. doi:10.1007/s11426-022-1347-9
16. Liu Z, Zhang Y, Shen N, Sun J, Tang Z, Chen X. Destruction of tumor vasculature by vascular disrupting agents in overcoming the limitation of EPR effect. *Adv Drug Deliv Rev*. 2022;183:114138. doi:10.1016/j.addr.2022.114138
17. Lippert JW. Vascular disrupting agents. *Bioorg Med Chem*. 2007;15(2):605–615. doi:10.1016/j.bmc.2006.10.020
18. Thorpe PE. Vascular targeting agents as cancer therapeutics. *Clin Can Res*. 2004;10(15):415–427. doi:10.1158/1078-0432.CCR-0642-03
19. Siemann DW. The unique characteristics of tumor vasculature and preclinical evidence for its selective disruption by tumor-vascular disrupting agents. *Cancer Treat Rev*. 2011;37(1):63–74. doi:10.1016/j.ctrv.2010.05.001
20. Wang K, Chen Q, Liu N, Zhang J, Pan X. Recent Advances in, and Challenges of, Anti-angiogenesis Agents for Tumor Chemotherapy Based on Vascular Normalization. *Drug Discov Today*. 2021;26(11):2743–2753. doi:10.1016/j.drudis.2021.07.024
21. Fruytier AC, Le Duff CS, Po C, et al. The blood flow shutdown induced by combretastatin A4 impairs gemcitabine delivery in a mouse hepatocarcinoma. *Front Pharmacol*. 2016;7:506. doi:10.3389/fphar.2016.00506
22. Li H, Zhou S, Wu M, et al. Light-driven self-recruitment of biomimetic semiconducting polymer nanoparticles for precise tumor vascular disruption. *Adv Mater*. 2023;35(24):e2210920. doi:10.1002/adma.202210920
23. Daei Farshchi Adli A, Jahanban-Esfahlan R, Seidi K, Samandari-Rad S, Zarghami N. An overview on Vadimezan (DMXAA): the vascular disrupting agent. *Chem Biol Drug Des*. 2018;91(5):996–1006. doi:10.1111/cbdd.13166
24. Wang Y, Yu H, Zhang D, et al. Co-administration of combretastatin A4 nanoparticles and sorafenib for systemic therapy of hepatocellular carcinoma. *Acta Biomater*. 2019;92:229–240. doi:10.1016/j.actbio.2019.05.028
25. Tang Z, X C. Tumor-targeting drug delivery systems based on Poly(L-glutamic acid)-g-Poly(ethylene glycol). *Acta Polymerica Sinica*. 2019;50 (6):543–552.
26. Li Z, Di C, Li S, Yang X, Nie G. Smart nanotherapeutic targeting of tumor vasculature. *Acc Chem Res*. 2019;52(9):2703–2712. doi:10.1021/acs.accounts.9b00283
27. Li B, Chu T, Wei J, et al. Platelet-membrane-coated nanoparticles enable vascular disrupting agent combining anti-angiogenic drug for improved tumor vessel impairment. *Nano Lett*. 2021;21(6):2588–2595. doi:10.1021/acs.nanolett.1c00168
28. Liu Zhi-Lin RX-T, Yue H, Jia-Li S, et al. A Novel CA4P polymeric nanoparticle for murine hepatoma therapy. *Chin J Poly Sci*. 2023;41 (8):1223–1229. doi:10.1007/s10118-023-2921-7
29. Zhilin Liu HZ, Sun J, Zheng M, et al. Organic-solvent-free "lego-like" modular preparation of fab-nondestructive antibody-drug conjugates with ultra-high drug-to-antibody ratio. *Adv Mater*. 2023. doi:10.1002/adma.202300377
30. Qin H, Yu H, Sheng J, et al. PI3Kgamma inhibitor attenuates immunosuppressive effect of poly(l-Glutamic Acid)-Combretastatin A4 Conjugate in metastatic breast cancer. *Adv Sci*. 2019;6(12):1900327. doi:10.1002/advs.201900327
31. He C, Hu Y, Yin L, Tang C, Yin C. Effects of particle size and surface charge on cellular uptake and biodistribution of polymeric nanoparticles. *Biomaterials*. 2010;31(13):3657–3666. doi:10.1016/j.biomaterials.2010.01.065
32. Kulkarni A, Chandrasekar V, Natarajan SK, et al. A designer self-assembled supramolecule amplifies macrophage immune responses against aggressive cancer. *Nat Biomed Eng*. 2018;2(8):589–599. doi:10.1038/s41551-018-0254-6

33. Strachan DC, R. B, Oei Y, Bissell MJ, Coussens LM, Pryer N. CSF1R inhibition delays cervical and mammary tumor growth in murine models by attenuating the turnover of tumor-associated macrophages and enhancing infiltration by CD8+ T cells. *OncoImmunology*. 2013;2(12):E26968. doi:10.4161/onci.26968
34. Rebelo SP, Pinto C, Martins TR, et al. 3D-3-culture: a tool to unveil macrophage plasticity in the tumour microenvironment. *Biomaterials*. 2018;163:185–197. doi:10.1016/j.biomaterials.2018.02.030
35. Zhu D, Johnson TK, Wang Y, et al. Macrophage M2 polarization induced by exosomes from adipose-derived stem cells Contributes to the exosomal proangiogenic effect on mouse ischemic hindlimb. *Stem Cell Res Ther*. 2020;11(1):162. doi:10.1186/s13287-020-01669-9
36. Cui X, Ma C, Vasudevaraja V, et al. Dissecting the immunosuppressive tumor microenvironments in glioblastoma-on-a-chip for optimized PD-1 immunotherapy. *Elife*. 2020;9. doi:10.7554/eLife.52253
37. Huang Y, Yang C, Lv J, et al. Formula optimization and in vivo study of poly(L-glutamic acid)-g-methoxy poly(ethylene glycol)/combretastatin A4/BLZ945 nanoparticles for cancer therapy. *Int J Pharm*. 2023;636:122849. doi:10.1016/j.ijpharm.2023.122849
38. Liu Z, Shen N, Tang Z, et al. An eximious and affordable GSH stimulus-responsive poly(alpha-lipoic acid) nanocarrier bonding combretastatin A4 for tumor therapy. *Biomater Sci*. 2019;7(7):2803–2811. doi:10.1039/C9BM00002J
39. Dan Peer JMK, Hong S, Farokhzad OC, Margalit R, Langer R, Langer R. Nanocarriers as an emerging platform for cancer therapy. *Nat Nanotechnol*. 2007;2:751–760. doi:10.1038/nnano.2007.387
40. Blanco E, Shen H, Ferrari M. Principles of nanoparticle design for overcoming biological barriers to drug delivery. *Nat Biotechnol*. 2015;33:941–951. doi:10.1038/nbt.3330
41. Xue X, Qu H, Li Y. Stimuli-responsive crosslinked nanomedicine for cancer treatment. *Exploration*. 2022;2(6):20210134. doi:10.1002/EXP.20210134
42. De Jong W, Borm PJA. Drug delivery and nanoparticles applications and hazards. *Int J Nanomedicine*. 2008;3(2):133–149. doi:10.2147/IJN.S596
43. Yeh YC, Creran B, Rotello VM. Gold nanoparticles: preparation, properties, and applications in bionanotechnology. *Nanoscale*. 2012;4(6):1871–1880. doi:10.1039/C1NR11188D
44. Boisselier E, Astruc D. Gold nanoparticles in nanomedicine: preparations, imaging, diagnostics, therapies and toxicity. *Chem Soc Rev*. 2009;38(6):1759–1782. doi:10.1039/b806051g
45. Liu L, Li S, Yang K, et al. Drug-free antimicrobial nanomotor for precise treatment of multidrug-resistant bacterial infections. *Nano Lett*. 2023;23(9):3929–3938. doi:10.1021/acs.nanolett.3c00632
46. Luntao Liu YW, Jiamin Y, Qinrui F, et al. Synthesis of magnesium nanoparticle for NIR-II-photoacoustic-imaging-guided synergistic burst-like and H2 cancer therapy. *Chem*. 2022;8(11):2990–3007. doi:10.1016/j.chempr.2022.07.001
47. Liu L, Li Q, Chen L, et al. Plasmon enhanced catalysis-driven nanomotors with autonomous navigation for deep cancer imaging and enhanced radiotherapy. *Chem Sci*. 2022;13(43):12840–12850. doi:10.1039/D2SC03036E
48. Gu B, Feng H, Dong J, Zhang H, Bian X, Liu Y. The establishment and characterization of a continuous cell line of mouse cervical carcinoma. *Chin J Clin Oncol*. 2008;5(1):44–48. doi:10.1007/s11805-008-0044-0
49. Feng CHEN, D. D, Yan FU, et al. Anti-tumor activity of biodegradable polymer-paclitaxel conjugated micelle against mice U14 cervical cancer. *Chem Res Chin Universi*. 2012;28(4):656–661.
50. Liu D, Duhamel J, Gauthier M. Synthesis and characterization of furan-based non-ionic surfactants (fbnios). *Langmuir*. 2023;39(26):8974–8983. doi:10.1021/acs.langmuir.3c00344
51. Negi SCK. Insight of molecular interactions between short-chain tetraalkylammonium bromides and cetyltrimethylammonium bromide: a spectroscopic and thermodynamic approach. *J Hazard Mater*. 2023;26(4):505–515.